Xiao *et al. Human Genomics* (2026) 20:85
https://doi.org/10.1186/s40246-026-00963-6

Human Genomics

RESEARCH Open Access

Integrated multiomics profiling of amniotic fluid exosomes reveals dysregulated lipid and protein signatures in fetal 22q11.2 deletion syndrome

Hai Xiao[1,2†], Tao Li[3,4†], Mengting Zhang[1,2†], Xue Lv[5], Yue Gao[1], Qiannan Guo[1], Zhenglong Guo[1], Hongdan Wang[1], Liangjie Guo[1], Hongyan Liu[1], Shixiu Liao[1] and Dong Wu[1,2*]

Abstract

Background Amniotic fluid exosomes (AF-Exos) are pivotal carriers of biological information during fetal development; however, their role in 22q11.2 Deletion Syndrome (22q11.2DS) remains unclear. To elucidate the molecular mechanisms underlying fetal anomalies in 22q11.2DS, this study performed a comprehensive multiomics analysis of AF-Exos obtained from 22q11.2DS fetuses (n = 5) and matched controls (n = 5).

Results While exosomal morphology and size distribution remained unaltered, integrated lipidomic and proteomic profiling revealed profound molecular remodeling. Lipidomics analysis revealed a specific suppression of diacylglycerols, triacylglycerols, and ceramides, accompanied by a shift in carbon chain length distribution. Concurrently, data-independent acquisition proteomics identified 329 differentially expressed proteins, highlighting a significant downregulation of PI4KA and widespread perturbations in pathways governing cardiovascular morphogenesis, angiogenesis, and SNARE-mediated vesicular transport. Integrated network analysis revealed strong correlations between the depletion of key lipids and reduced abundance of PI4KA and SNARE complex components, suggesting a potential interplay between lipid metabolism and vesicle trafficking.

Conclusions These findings, extending beyond the primary genetic driver *TBX1*, point to distinct alterations in lipid signaling and exosomal transport machinery in 22q11.2DS, suggesting a novel parallel pathogenic mechanism. This study provides a novel multiomics resource for understanding 22q11.2DS pathogenesis and generates valuable hypothesis-driven candidates for future mechanistic investigation.

Keywords 22q11.2 deletion syndrome, PI4KA, Amniotic fluid exosomes, Lipidomics, Proteomics

†Hai Xiao, Tao Li and Mengting Zhang authors have contributed equally to this work.

*Correspondence:
Dong Wu
regalyang@163.com
[1]Institute of Medical Genetics, Henan Provincial People's Hospital, No. 7 Weiwu Road, Zhengzhou 450003, Henan, China
[2]NHC Key Laboratory of Birth Defects Prevention, Institute of Reproductive Health, Henan Academy of Innovations in Medical Science, Zhengzhou 451163, Henan, China
[3]Henan Neurodevelopment Engineering Research Center for Children, Children's Hospital Affiliated to Zhengzhou University, Henan Children's Hospital Zhengzhou Children's Hospital, Zhengzhou 450018, China
[4]Tianjian Laboratory of Advanced Biomedical Sciences, Academy of Medical Sciences, Zhengzhou University, Zhengzhou 450066, China
[5]Health Management Center, Henan Provincial People's Hospital, Zhengzhou 450003, Henan, China

Introduction

22q11.2 Deletion Syndrome (22q11.2DS), also known as DiGeorge syndrome, is the most common chromosomal microdeletion disorder in humans, with an estimated prevalence of 1 in 3000–6000 live births [1]. The syndrome is characterized by a highly heterogeneous clinical phenotype, primarily manifesting as congenital heart defects (particularly conotruncal anomalies), palatal abnormalities, immunodeficiency, and neurodevelopmental delays [2–4]. While haploinsufficiency of the *TBX1* gene is well-established as a primary genetic driver [5], genetic deletion alone does not fully account for the complex metabolic perturbations and phenotypic variability observed in patients. Furthermore, current mechanistic insights are largely derived from postnatal studies or animal models [6]; consequently, the molecular pathology during the critical window of intrauterine fetal development remains unexplored.

Amniotic fluid (AF) constitutes the immediate environment for the developing fetus, accumulating biological signals derived from the fetal skin and respiratory, gastrointestinal, and urinary tracts [7]. Amniotic fluid exosomes (AF-Exos), nanoscale extracellular vesicles (30–150 nm) [8], have emerged as key mediators of intercellular communication within this complex fluid [9]. By encapsulating a diverse cargo of proteins, lipids, and nucleic acids, AF-Exos serve as dynamic indicators of the fetus's physiological and pathological status [10]. Emerging evidence indicates that AF-Exos play pivotal roles in regulating essential processes such as angiogenesis, inflammation, and neurogenesis [11, 12]. Consequently, characterizing the molecular landscape of AF-Exos in 22q11.2DS presents a unique opportunity to elucidate fetal pathogenesis.

Despite advances in genomic and transcriptomic profiling of 22q11.2DS, the metabolic and functional characterization of 22q11.2DS exosomes remains poorly understood. Exosomes are not merely inert protein carriers; their lipid membrane composition determines the biophysical properties, such as curvature and fluidity, which strictly dictate vesicle biogenesis, secretion, and fusion with target cells [13]. The interplay between lipids and membrane-associated proteins—particularly the SNARE complex involved in vesicular transport—is central to cellular signaling [14]. The *PI4KA* gene, located within the 22q11.2 deletion region, encodes a phosphatidylinositol kinase that is essential for lipid signaling. However, whether the loss of *PI4KA* leads to systemic lipidomic remodeling and disrupts exosome-mediated signaling in 22q11.2DS fetuses remains unknown.

To address these gaps, this study employed an intergrated multiomics strategy, combining untargeted lipidomics and Data-Independent Acquisition (DIA) quantitative proteomics, to profile AF-Exos from fetuses with 22q11.2DS and matched controls. The primary aims of this study were to characterize specific AF-Exos lipid and protein signatures, elucidate critical regulatory networks linking *PI4KA* to glycerolipids and ceramides, and propose mechanistic links between vesicular transport dysfunction and developmental anomalies. These findings represent the first comprehensive multiomics map of AF-Exos in 22q11.2DS, providing novel insights into fetal pathophysiology and highlighting potential molecular pathways for future functional investigation.

Materials and methods

Study design

To elucidate the role of exosomes in fetal growth and development in 22q11.2DS, we employed a systematic workflow that integrated clinical sampling, multiomics analysis, and targeted validation (Fig. 1). Amniotic fluid samples were obtained from five fetuses with 22q11.2DS and five matched normal controls, after which exosomes were isolated using a magnetic bead-based method. Following morphological and physical characterization, molecular alterations were profiled via untargeted lipidomics and DIA-based quantitative proteomics. Integrated analysis of these datasets identified key dysregulated pathways, and selected protein targets were validated by Parallel Reaction Monitoring (PRM).

Study participants and amniotic fluid sample collection

This study was approved by the Ethics Committee of the Henan Provincial Peoples Hospital (Approval No.

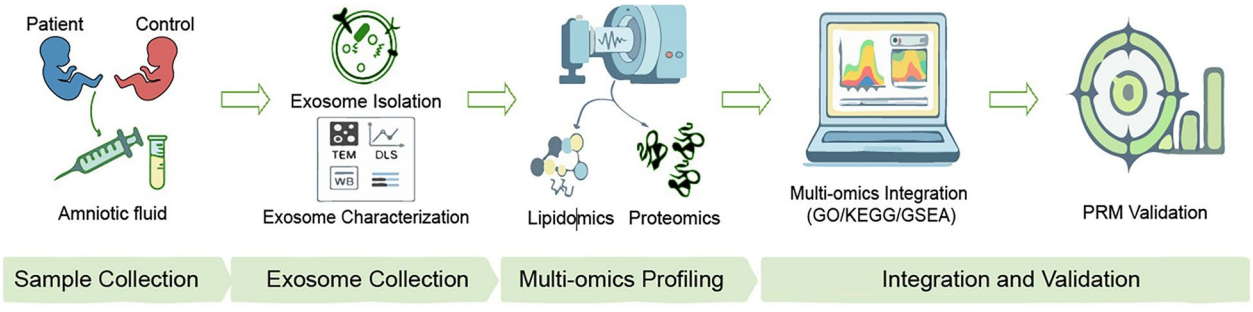

Fig. 1 Schematic illustration of the study design and multiomics workflow

2019-134) and conducted in accordance with the Declaration of Helsinki. Written informed consent was obtained from all participants. The study included five fetuses with confirmed 22q11.2DS and five matched controls verified by chromosomal microarray analysis to be free of chromosomal abnormalities (Fig. 2). Two independent operators performed fetal echocardiographic assessments according to the American Society of Echocardiography guidelines. All fetuses with 22q11.2DS exhibited cardiac anomalies during the second trimester (Table 1). NO participants had other medical conditions or pregnancy complications affecting fetal development. Maternal age, gestational age, and BMI were comparable between the groups (Table 2). Approximately 20 mL of amniotic fluid was collected from each participant via ultrasound-guided amniocentesis. The samples were subsequently centrifuged at 2000 × g for 10 min at 4 °C to remove cells and debris, and the supernatants were stored at – 80 °C until exosome isolation.

Exosome isolation and characterization

AF-Exos isolation

AF-Exos were isolated using a magnetic bead-based enrichment strategy described previously [15]. Thawed samples were centrifuged at 2000 × g for 30 min, followed by 12,000 × g for 45 min at 4 °C to remove apoptotic bodies. The supernatant was filtered through a 0.22 μm pore filter (Sigma-Aldrich, USA). Exosome enrichment was performed using functionalized magnetic beads (Mag-CS; Untangled Bio, China) according to the manufacturers protocol. Samples were incubated with Mag-CS

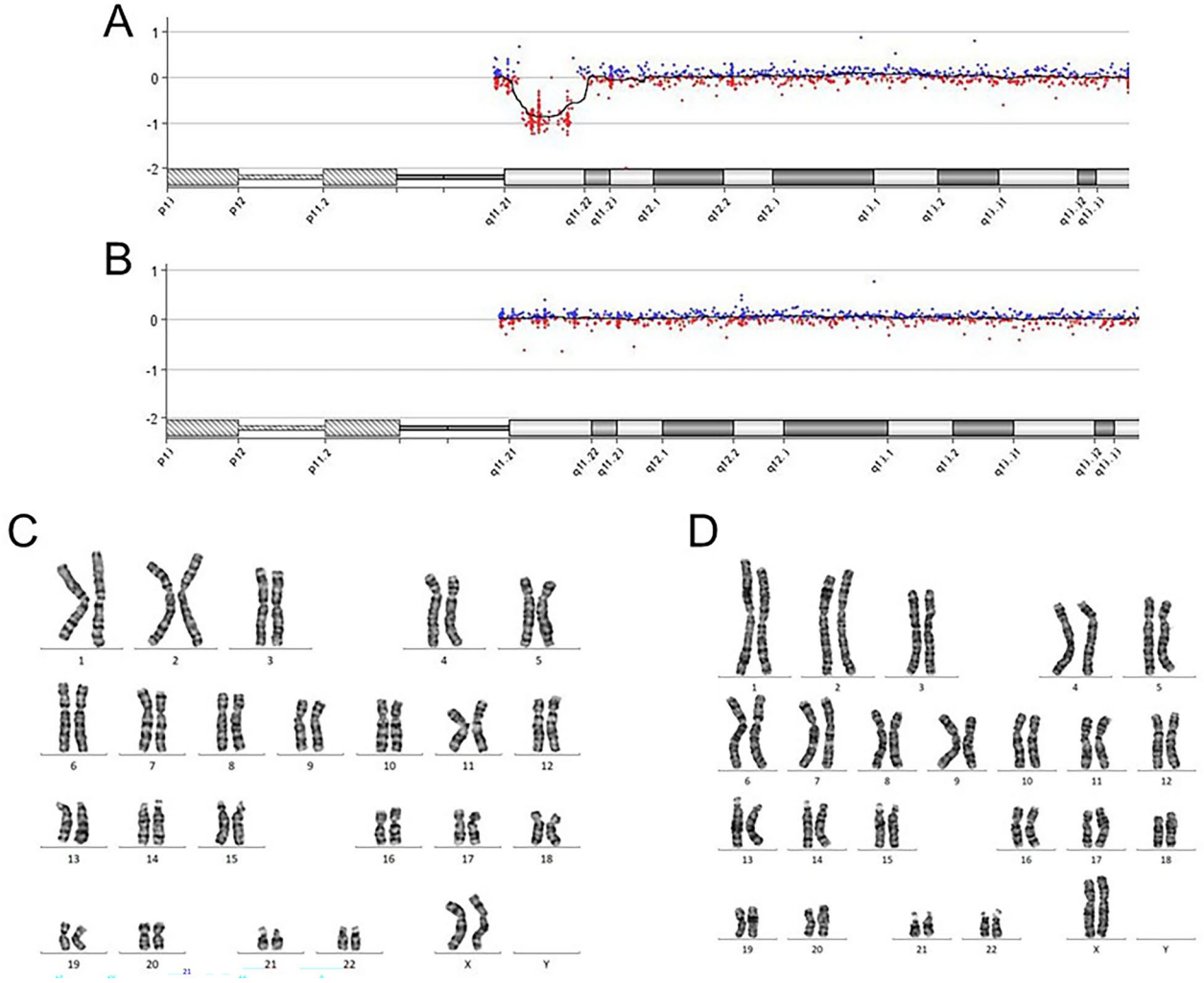

Fig. 2 Cytogenetic validation of study participants. **A** Representative array comparative genomic hybridization (aCGH) profile of a fetus with 22q11.2 deletion syndrome. The deflection in the log2 ratio (black line) indicates a specific copy number loss (microdeletion) in the 22q11.2 region. **B** Representative aCGH profile of a normal control fetus showing a balanced copy number in the corresponding chromosomal region. **C**, **D** Standard G-banded karyotypes of the 22q11.2DS fetus (**C**) and normal control (**D**). These analyses were performed to exclude other gross chromosomal aneuploidies or structural abnormalities (resolution: 400–550 bands)

Table 1 Clinical indications and cytogenetic findings of the study participants

Case ID	Indications for prenatal diagnosis	Karyotype	CMA results (hg19)
P1	RAA with ALSA	46,XY	22q11.21(18,894,835_21,440,514)×1
P2	VSD, aortic override, pulmonary stenosis	46,XX	22q11.21(18,894,835_21,440,514)×1
P3	Family history of CHD; RAA with ALSA	46,XX	22q11.21(18,894,835_21,505,417)×1
P4	Cardiac anomaly; RAA with ALSA	46,XX	22q11.21(18,894,835_20,311,763)×1
P5	Bilateral hydronephrosis, short nasal bone, VSD, PLSVC	46,XX	22q11.21(18,894,835_21,505,417)×1
C1	High risk for Down syndrome (serum screening)	46,XY	–
C2	Evaluation post-amniocentesis	46,XX	–
C3	High risk on NIPT	46,XX	–
C4	Advanced maternal age; IVF pregnancy	46,XX	–
C5	Advanced maternal age	46,XX	–

CMA, chromosomal microarray analysis; RAA, right aortic arch; ALSA, aberrant left subclavian artery; VSD, ventricular septal defect; CHD, congenital heart disease; PLSVC, persistent left superior vena cava; NIPT, non-invasive prenatal testing; IVF, in vitro fertilization; –, No pathogenic CNVs detected. Genomic coordinates are based on the GRCh37/hg19 assembly

Table 2 Demographic and clinical characteristics of the study participants

Parameter	22q11.2DS	Control	*P*-value
Maternal age (years)	30.8 ± 4.44	32.8 ± 7.7	0.63
Gestational age (weeks)	23.2 ± 1.92	23.2 ± 1.79	1.00
BMI (kg/m^2)	20.26 ± 1.4	21.02 ± 1.57	0.44

(2 mg/mL) for 1 h at room temperature with rotation, washed with PBS, and eluted for downstream analysis.

Transmission electron microscopy (TEM)

Exosome morphology was visualized using TEM. Briefly, 20 µL of the sample was mixed with 20 µL of 4% paraformaldehyde and fixed onto a 200-mesh carbon-coated copper grid (BZ11022A; Beijing Zhongjingkeyi Technology, China) for 30 min. After washing with ultrapure water, the grids were negatively stained with 2% uranyl acetate for 30 s. Air-dried grids were imaged using a JEM-1400 transmission electron microscope (JEOL, Tokyo, Japan).

Dynamic light scattering (DLS)

Particle size distribution was determined using DLS. The exosome samples were diluted in PBS (pre-filtered through a 0.22 µm membrane) and loaded into a disposable cuvette. Measurements were performed using a Zetasizer Nano ZS90 instrument (Malvern Panalytical, UK). The data were analyzed using the Zetasizer Software to generate the intensity-based hydrodynamic size distribution.

Western blot analysis

To validate exosome enrichment, total proteins were extracted, separated by SDS-PAGE, and transferred onto polyvinylidene fluoride membranes. Membranes were probed with antibodies against canonical markers: Alix (Abcam, ab186429, dilution 1:1000), CD9 (Abcam, ab92726, 1:1000), CD63 (Abcam, ab134045, 1:500), and TSG101 (Abcam, ab125011, 1:1000). Protein bands were visualized using an enhanced chemiluminescence (ECL) system.

Non-targeted lipidomics analysis

Lipids were extracted using methyl-tert-butyl ether (MTBE). The sample (25 µL) was mixed with an extraction reagent containing internal standards, vortexed, and centrifuged. The supernatant was filtered prior to LC–MS/MS analysis. Lipidomic profiling was performed using a Thermo Vanquish UHPLC system coupled to a Q Exactive Plus Orbitrap mass spectrometer (Thermo Fisher Scientific, USA). Separation was achieved on an Acquity BEH C18 column (1.7 µm, 2.1 × 100 mm) at 40 °C. The mobile phase consisted of (A) 40:60 water: acetonitrile and (B) 90:10 isopropanol: acetonitrile, both with 10 mM ammonium formate and 0.1% formic acid. Gradient elution (30–100% B over 20 min) was used. MS data were acquired in the Data-Dependent Acquisition (DDA) mode (positive/negative switching). Key parameters: resolution 70,000 (MS1)/17,500 (MS2); HCD energy 20/30%; scan range m/z 200–1800. Lipid identification and quantification were performed using the MS-DIAL software (v4.70).

Protein digestion and peptide preparation

Proteins were denatured in 8 M ammonium bicarbonate, reduced with 10 mM dithiothreitol (DTT) for 30 min at 37 °C, and alkylated with 20 mM iodoacetamide (IAM) for 30 min in the dark. Samples were diluted and digested sequentially with Lysyl Endopeptidase (LysC) (1 µg, 2 h at 37 °C) and Trypsin (1 µg, overnight at 37 °C). The reaction was quenched using 10% trifluoroacetic acid (TFA). The peptides were desalted using SoLAµ HRP plates and reconstituted in 0.1% formic acid for analysis.

DIA proteomics

Peptides were analyzed using a Thermo Ultimate 3000 RSLCnano system coupled to a Q Exactive HF-X Orbitrap mass spectrometer. Separation was performed on a trap column and an analytical column (75 µm × 25 cm) using a 65-min gradient. The mass spectrometer was operated in the DIA mode. Full MS scans were acquired at 60,000 resolution, followed by DIA scans with 40

variable isolation windows at 30,000 resolution. Raw data were processed using DIA-NN software (v1.8.1) against a human proteome database (FDR < 1%).

Validation via parallel reaction monitoring (PRM)

To validate the DIA results, 15 candidate proteins were selected based on three criteria: (1) localization within the 22q11.2 microdeletion region (PI4KA, TBX1); (2) integral roles in the SNARE vesicular transport pathway (STX3); and (3) involvement in cardiovascular morphogenesis, extracellular matrix remodeling, and related downstream signaling pathways (MMP2, ITGA2, COL6A3, TIMP2, SPP1, THBS4, MYL9, PRKACA, INSR, GNG12, PRL, and ATF6B). Due to the limited volume of AF-Exos remaining after exhaustive multiomics profiling, targeted PRM quantification was performed on a subset of the discovery cohort (n = 4/group). The PRM method combined two scan events, comprising a full-scan event and targeted MS/MS scans for precursor ions, based on a scheduled precursor inclusion list with an 8-min retention time window. The full scan was acquired over a mass range of m/z 350–1500 with a resolution of 45,000 (Full Width at Half Maximum at m/z 200), an automatic gain control (AGC) target value of 3E6, and a maximum injection time of 20 ms. The PRM scans were acquired at a resolution of 30,000 (Full Width at Half Maximum at m/z 200) with an AGC target value of 1E5 and a maximum injection time of 100 ms. Targeted peptides were isolated using a 1.0 m/z isolation window, and fragmentation was performed using Higher-energy Collisional Dissociation with a normalized collision energy of 27.

Bioinformatics and statistical analysis

Data were normalized to correct for systematic variations. To minimize the impact of outliers given the sample size, Fold Change (FC) was calculated based on median intensity values in the 22q11.2DS and control groups. Differentially Expressed Proteins (DEPs) were identified with a threshold of $|FC| \geq 1.5$ and an FDR < 0.01. Similarly, differentially expressed lipids (DELs) were defined as those with $|FC| \geq 1.2$ and $P < 0.05$. Functional enrichment analysis (GO and KEGG) was performed using ClusterProfiler (v3.18). Gene Set Enrichment Analysis (GSEA) was performed using the WebGestalt 2024 [16] online toolkit (http://www.webgestalt.org), based on ranked proteins list. Protein–Protein Interaction (PPI) networks were constructed using the STRING database (confidence score > 0.4) and visualized with Cytoscape to identify key functional modules. Lipid composition and carbon chain length distribution were analyzed using LipidSig (v1.0.3) [17, 18] (http://chenglab.cmu.edu.tw/lipidsig). Multivariate analyses (PCA and PLS-DA) and hierarchical clustering were visualized using R packages. Integrated pathway analysis of DEPs and DELs was conducted using MetaboAnalyst 6.0 [19] (https://www.metaboanalyst.ca). Correlation analysis between DEPs and DELs was performed using Spearmans rank correlation coefficients. Demographic data were compared using Students t-test or Fishers exact test, with $P < 0.05$ considered statistically significant.

Results

Characterization of AF-Exos

Before omics profiling, AF-Exos were characterized according to the MISEV guidelines [20]. TEM analysis demonstrated that particles from both the 22q11.2DS and control groups exhibited a characteristic cup-shaped morphology with well-defined membranes (Fig. 3A, B). Western blotting confirmed the presence of canonical exosomal markers CD63, CD9, TSG101, and Alix (Fig. 3C). DLS analysis indicated a size distribution peaking at approximately 130 nm (Fig. 3D). Statistical evaluation revealed no significant difference in the mean particle size between the two groups (Fig. 3E).

Lipidomic profiling of AF-Exos

Untargeted lipidomics was performed on AF-Exo samples (n = 5 per group) to define lipidomic signature in 22q11.2DS. The comprehensive list of all identified lipids, including fold changes and statistical *P*-values, is provided in Supplementary Table S1. Principal Component Analysis (PCA) confirmed detection stability, evidenced by the tight clustering of quality control (QC) samples, and revealed a distinct separation between the 22q11.2DS and control groups (Fig. 4A). Relative abundance analysis revealed that glycerolipids and glycerophospholipids were the dominant lipid classes in both exosome populations, followed by sphingolipids (Fig. 4B). The overall lipid saturation profiles (total double bonds) were comparable between the groups (Fig. 4C). The 22q11.2DS group exhibited specific shifts in carbon chain length distributions: a reduced relative abundance of lipid with 30–40 carbon and a concomitant increase in ultra-long-chain species (> 50 carbons) (Fig. 4D). Differential expression analysis identified 11 significantly downregulated lipid molecules, primarily diacylglycerols (DG), triacylglycerols (TG), and ceramides (Cers). Hierarchical clustering corroborated these findings, illustrating the consistent suppression of specific species, including DG 26:3, DG 28:3, and several TG and Cer variants, within the 22q11.2DS samples (Fig. 4E, F).

Proteomic profiling of AF-Exos

DIA proteomics identified 329 DEPs (187 upregulated and 142 downregulated), indicating significant molecular remodeling. The complete list of all identified proteins, along with their detailed fold changes, *P*-values, and adjusted *P*-values, is detailed in Supplementary Table S2.

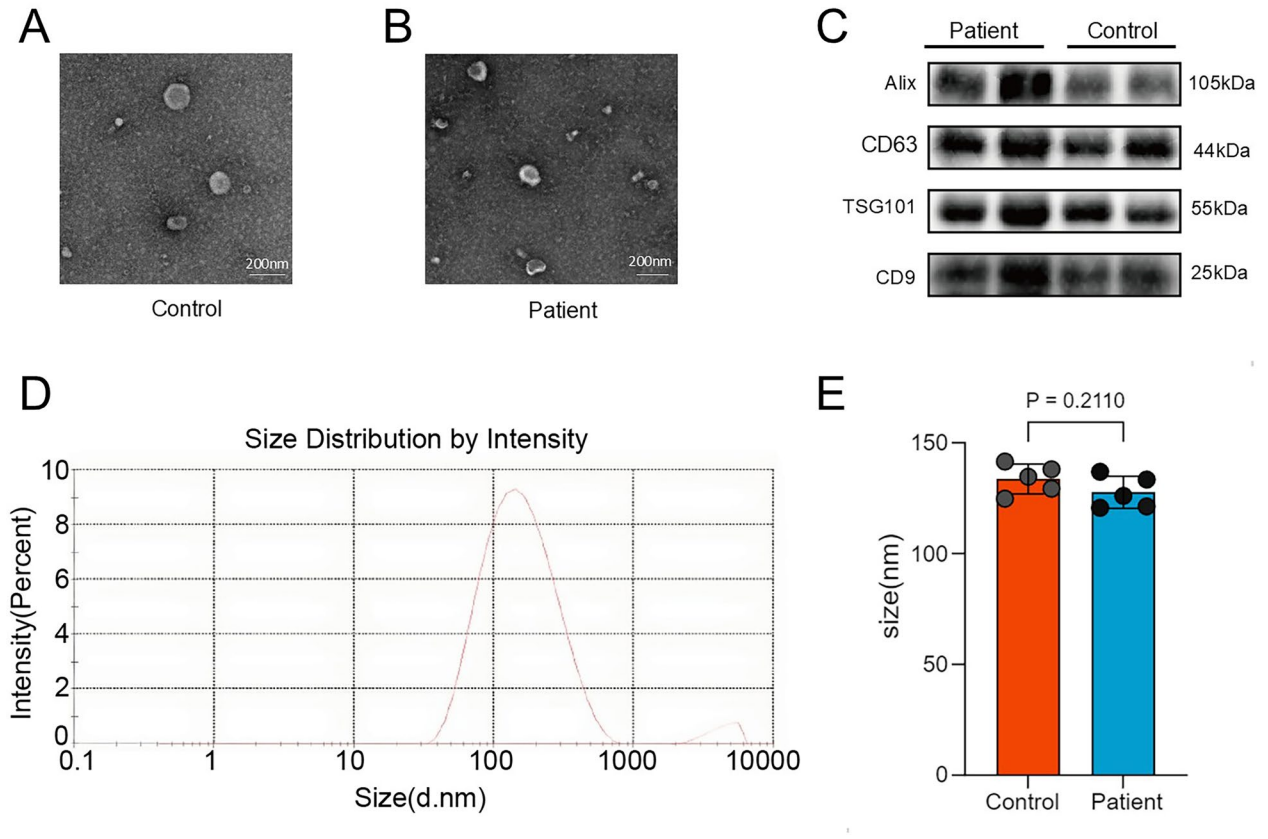

Fig. 3 Characterization of AF-Exos from Control and 22q11.2DS pregnancies. **A**, **B** Representative transmission electron microscopy (TEM) images of exosomes isolated from the control (**A**) and patient groups (**B**). Scale bar = 200 nm. **C** Western blot analysis of exosomal markers (Alix, CD63, TSG101, and CD9) in the isolated fractions from the Patient and Control groups. **D** Representative size distribution profile of exosomes measured by Dynamic Light Scattering (DLS). **E** Statistical comparison of the mean particle size between the Control and Patient groups (n = 4 per group). Data are presented as mean ± standard deviation (SD). The *P* value was determined using an unpaired Students t-test ($P = 0.2110$)

Among the 22q11.2DS-associated candidates (PI4KA, COMT, and SERPIND1), all exhibited downward trends; however, only PI4KA demonstrated a statistically significant reduction ($P < 0.05$) (Fig. 5A). Hierarchical clustering analysis segregated the patient and control groups into distinct clusters, demonstrating the significant and consistent remodeling of the exosomal proteome associated with 22q11.2DS (Fig. 5B). GO enrichment analysis further clarified the biological functions of the DEPs (Fig. 5C). Within the Biological Process (BP) category, notable enrichment of terms essential for cardiovascular morphogenesis was observed, particularly blood vessel development and angiogenesis. Additionally, pathways regulating cell movement, such as those involved in the positive regulation of cell motility and migration, were significantly enriched. Within the Cellular Component (CC) category, the DEPs were predominantly localized to the extracellular matrix, focal adhesion sites, and lumen of secretory granules. Furthermore, KEGG pathway enrichment analysis revealed that SNARE interactions in vesicular transport was the most significantly enriched pathway, followed by protein processing in the endoplasmic reticulum and endocytosis. The analysis further indicated enrichment within cardiovascular-related signaling pathways, particularly the PI3K-Akt signaling pathway and hypertrophic cardiomyopathy (Fig. 5D).

Integrated multiomics and network analysis

To mechanistically integrate our lipidomic and proteomic findings, we constructed a PPI network. This analysis identified two central modules: one centered on the SNARE vesicular trafficking machinery (STX3, VAMP3/8, and SNAP23), ADAM10, and CD9, and the second comprising the CCM vascular signaling complex (CCM2 and PDCD10) associated with SQSTM1 and PRKCZ (Fig. 6A). Joint pathway analysis, integrating both DEPs and DELs, identified fatty acid degradation and glycerolipid metabolism as the pathways with the highest impact and statistical significance. Sphingolipid metabolism, glycerophospholipid metabolism, and inositol phosphate metabolism were also identified as significantly affected pathways (Fig. 6B). We examined the associations between specific protein candidates and major lipid classes using Pearsons correlation analysis.

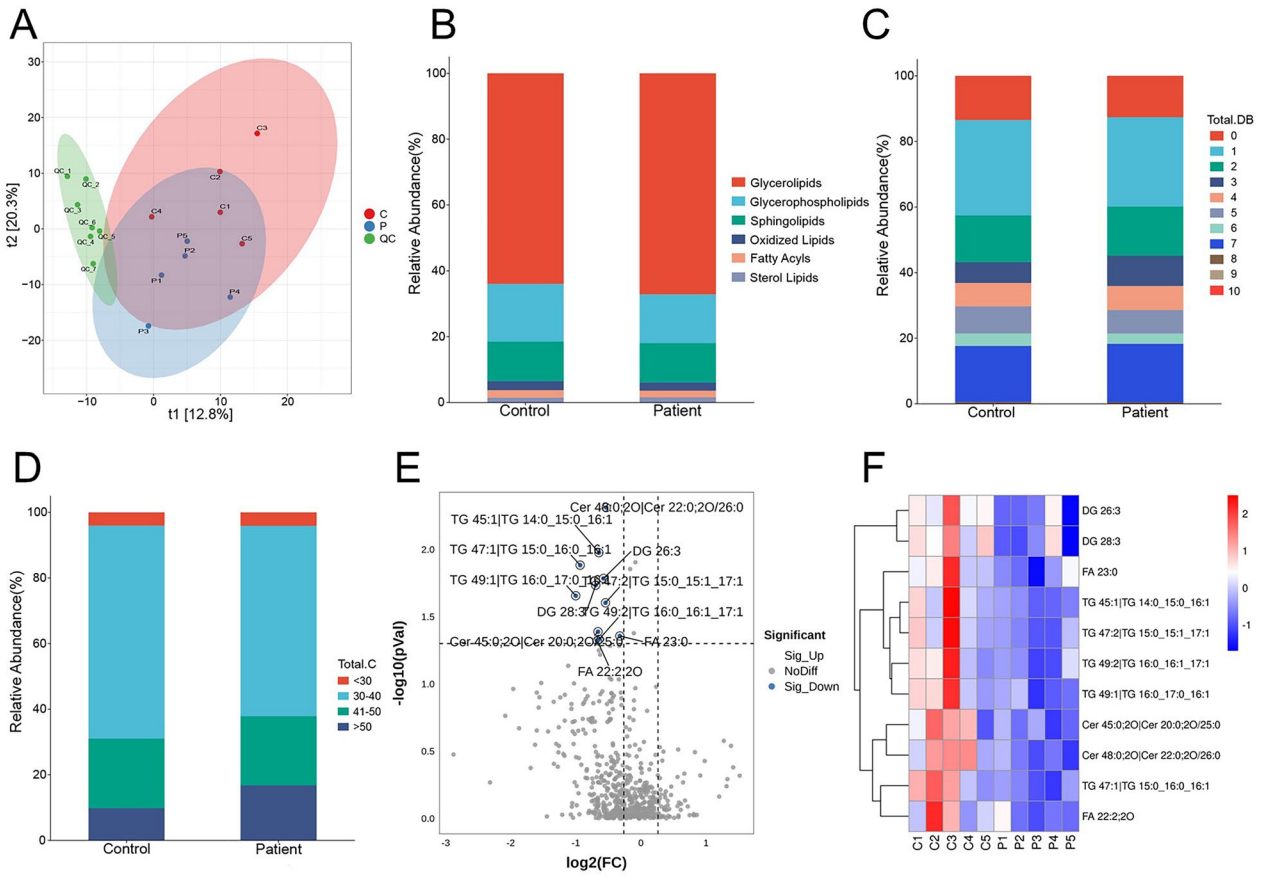

Fig. 4 Lipidomic landscape of AF-Exos in 22q11.2DS (n = 5) and control (n = 5) groups. **A** Principal Component Analysis (PCA) score plot showing the separation trend between the control (red) and patient (blue) groups. **B** Stacked bar chart showing the relative abundance of major lipid classes. **C** Distribution of lipids based on the total number of double bonds. **D** Distribution of lipids based on the total carbon chain length. Note the decrease in the 30–40 carbon fraction and the increase in the > 50 carbon fraction in the patient group. **E** Volcano plot visualizing the differentially expressed lipids ($P < 0.05$, fold change (FC) > 1.2 or < 0.83). The x-axis represents the log2(patient/control) ratio. Blue dots indicate significantly downregulated lipids (mainly DG, TG, and Cer) in the patient group. **F** Hierarchical clustering heatmap showing the distinct downregulation of specific lipid species in 22q11.2DS

Positive correlations were observed between the abundance of Total Diglycerides (TotalDG), Total Ceramides (TotalCER), and Total Triglycerides (TotalTG) and the expression levels of PI4KA, SNARE complex proteins (STX3, SNAP23), and vascular regulators (CCM2, ITGA2). Conversely, CDH2 was negatively correlated with these lipid classes (Fig. 6C). Gene Set Enrichment Analysis (GSEA) showed a significant downregulation of pathways associated with synaptic signaling (GABAergic and Glutamatergic synapses) and endocytosis in the 22q11.2DS group (Fig. 6D). The specific enrichment plot for the endocytosis pathway confirmed this trend, exhibiting a negative enrichment score (ES) of – 0.46 (Fig. 6E).

PRM validation of key candidates

Fifteen proteins, including PI4KA and TBX1, were selected for PRM validation. TBX1 was undetectable in both cohorts, likely due to low abundance. The quantitative results for the remaining 14 proteins are presented in Fig. 7. Although most proteins did not reach statistical significance-likely attributable to the limited sample size-GNG12 showed a significant alteration. Nevertheless, the expression trends of key proteins, such as PI4KA and STX3, were consistent with the proteomics data, corroborating our initial findings.

Discussion

While research on pathogenic mechanisms in 22q11.2DS has predominantly focused on the transcription factor *TBX1* [21], this protein was undetectable in AF-Exos in our study, likely due to its low abundance or predominant nuclear localization [22]. While *TBX1* remains the primary genetic driver, our integrated multiomics analysis suggests a potential parallel or downstream pathogenic mechanism involving exosomal lipidome remodeling and membrane trafficking defects. We hypothesize that these processes may be influenced by the haploinsufficiency of the lipid kinase *PI4KA*, reflecting cytoplasmic and membrane-associated perturbations rather than direct transcriptional dysregulation.

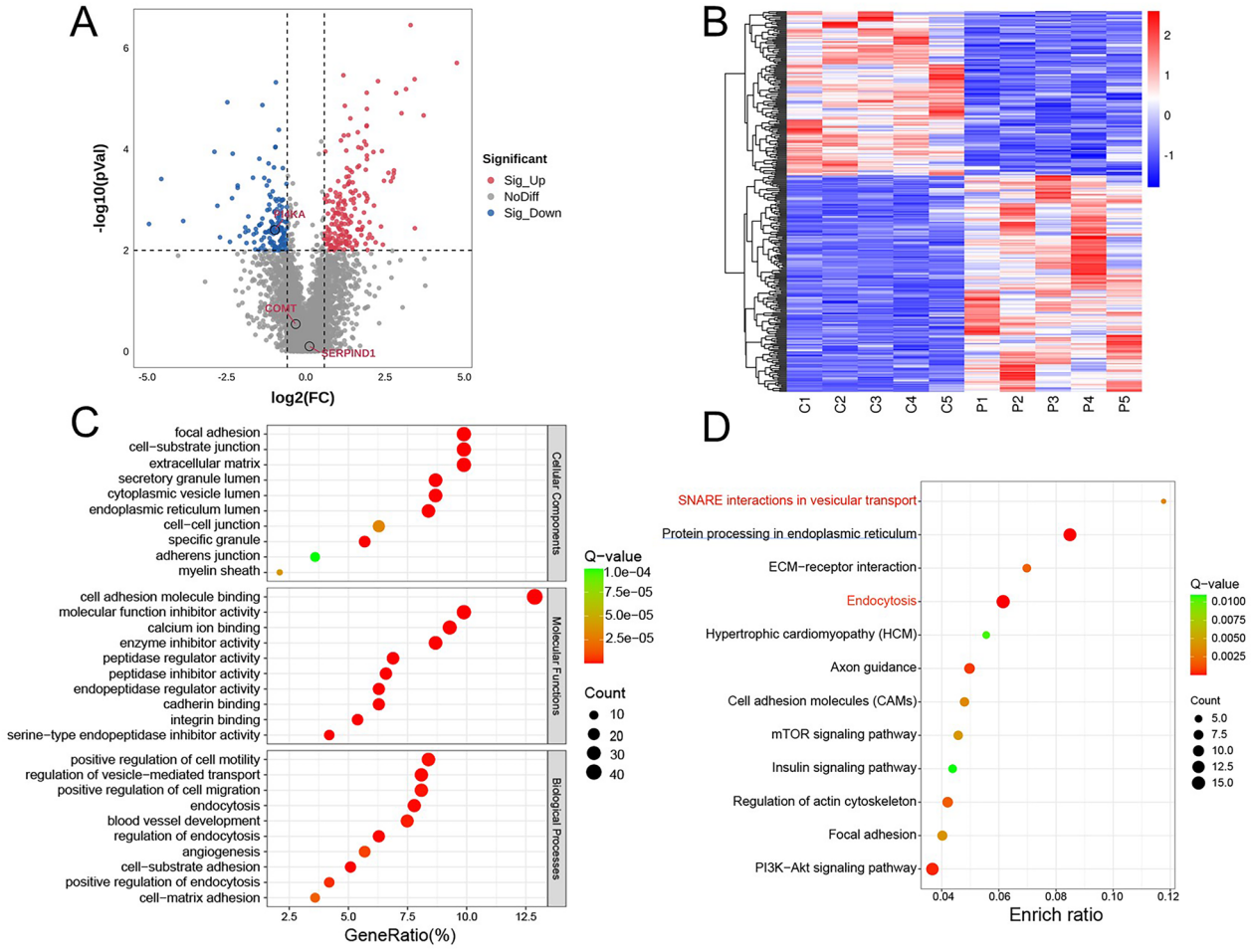

Fig. 5 Proteomic profiling reveals global protein alterations and pathway dysregulation in 22q11.2DS AF-Exos. **A** Volcano plot visualizing differentially expressed proteins (DEPs). The x-axis represents the log2(patient/control) fold change, and the y-axis represents the-log10 (*P*-value). Red and blue dots indicate significantly upregulated and downregulated proteins, respectively. Key proteins encoded by genes in the 22q11.2 deletion region (PI4KA, COMT, and SERPIND1) are indicated. **B** Hierarchical clustering heatmap of DEPs showing distinct separation and expression patterns between the control (C1–C5) and patient (P1–P5) groups. Red indicates high expression, and blue indicates low expression of the indicated genes. **C** Gene Ontology (GO) enrichment analysis of DEPs classified by Cellular Component, Molecular Function, and Biological Process. The dot size represents the gene count, and the color gradient represents the Q-value. **D** KEGG pathway enrichment analysis of DEPs. The size of the bubbles represents the number of proteins enriched in each pathway, and the color indicates the statistical significance (Q-value). Notably, SNARE interactions were significantly enriched in vesicular transport and endocytosis pathways

Quantitative proteomic profiling revealed a significant downregulation of PI4KA in amniotic fluid exosomes from 22q11.2DS fetuses. This haploinsufficiency is potentially associated with a cascade that limits the synthesis of the downstream signaling molecule phosphatidylinositol 4,5-bisphosphate (PIP2) [23]. Given PIP2s role as a direct substrate for phospholipase C, its reduced availability would theoretically limit DG generation [24]. This mechanism would be consistent with the observed lipidomic signature in patient-derived exosomes, which showed specific downregulation of medium-chain unsaturated diacylglycerols (DG 26:3 and DG 28:3) and significant suppression of glycerolipid metabolism pathways, as shown in Fig. 4E, F. Biophysically, the depletion of these conical-shaped lipids may impair the membranes ability to generate local negative curvature, a physical prerequisite for vesicle budding and fission [25]. Furthermore, lipid chain length analysis revealed the enrichment of very-long-chain lipids (> 50 carbon atoms), which are known to enhance membrane order and rigidity through chain interdigitation [26]. Consequently, the reduction in curvature-inducing DG combined with an increase in rigid lipids can physically elevate the energy barrier for membrane deformation, thereby potentially limiting the efficiency of vesicle biogenesis.

Consistent with established biophysical principles linking membrane curvature to vesicle fusion [27], our data revealed a concurrent depletion of curvature-inducing lipids and SNARE components. This raises the possibility that the observed lipidome remodeling could

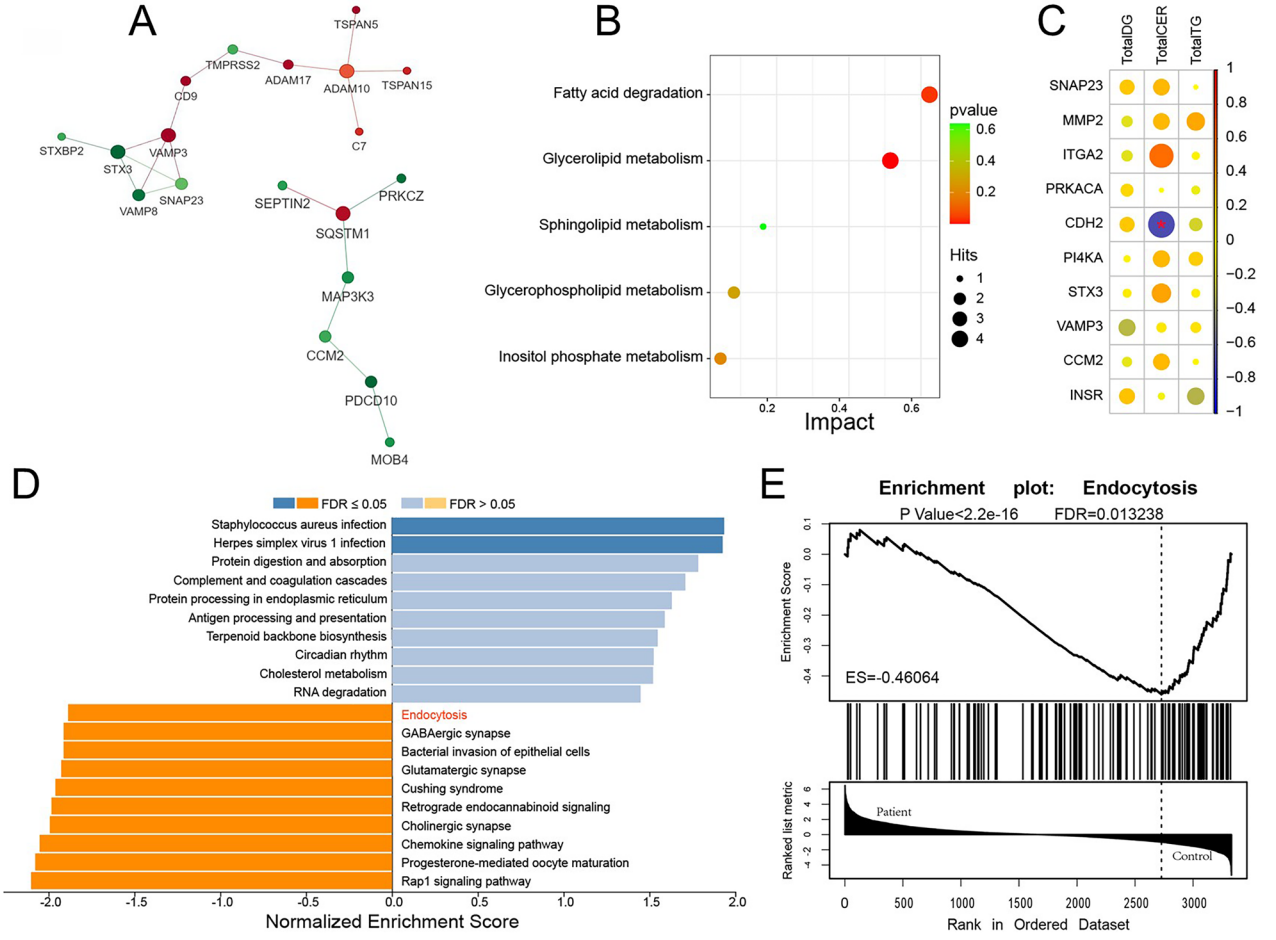

Fig. 6 Integrated multiomics network analysis reveals convergent dysregulation of vesicle trafficking and signaling modules. **A** Protein–protein interaction (PPI) network constructed from differentially expressed proteins. The network revealed functional clusters involving SNARE components (e.g., STX3, VAMP8, and SNAP23) and vascular stability proteins (CCM2 and PDCD10). Node colors represent differential expression (Green: Downregulated; Red: Upregulated). **B** Joint pathway analysis of DEPs and DELs. The scatter plot displays the metabolic pathways plotted by pathway impact (x-axis) and statistical significance (color scale). The bubble size corresponds to the number of molecules (hits) matched within each pathway. **C** Pearson correlation matrix showing the relationship between key proteins (rows) and total lipid classes (TotalDG, TotalCER, and TotalTG; columns). The circle size and color intensity indicate the strength and direction of the correlation coefficient, with yellow/orange representing positive correlations and blue/purple representing negative correlations. **D** Gene Set Enrichment Analysis (GSEA) bar chart displaying Normalized Enrichment Scores (NES). Orange bars indicate pathways significantly downregulated in the patient group (FDR < 0.05). **E** GSEA enrichment plot for the endocytosis pathway, showing a significantly negative enrichment score (ES = −0.46, FDR = 0.013) in the patient group

create a non-permissive biophysical environment that may impede SNARE assembly. This is supported by our proteomic analysis, which highlighted the SNARE interactions in vesicular transport pathway as a key target, driven by the downregulation of essential effectors like STX3 and VAMP8.

Dysfunction of the SNARE machinery is expected to block key signaling pathways dependent on vesicular transport [28]. Notably, our data revealed a paradoxical upregulation of the metalloprotease ADAM10 and the scaffold protein, SQSTM1. This pattern could be interpreted as a trafficking blockade, where vesicles stall and are released non-specifically [29]. While we cannot exclude the possibility that the upregulation of ADAM10 and SQSTM1 represents a compensatory cellular stress response to impaired fusion machinery or lysosomal dysfunction, the concurrent downregulation of SNARE supports the trafficking defect hypothesis; however, distinguishing between accumulation and increased synthesis requires further cellular validation. Under physiological conditions, ADAM10 requires precise SNARE-mediated fusion to reach the plasma membrane (PM) [14]. In 22q11.2DS, the putative failure of vesicle fusion may cause ADAM10-containing vesicles to stall and accumulate intracellularly, potentially contributing to their subsequent non-specific release through exosomes [30]. Consequently, although ADAM10 is abundant in exosomes, it is likely mislocalized and functionally inert in its canonical signaling roles.

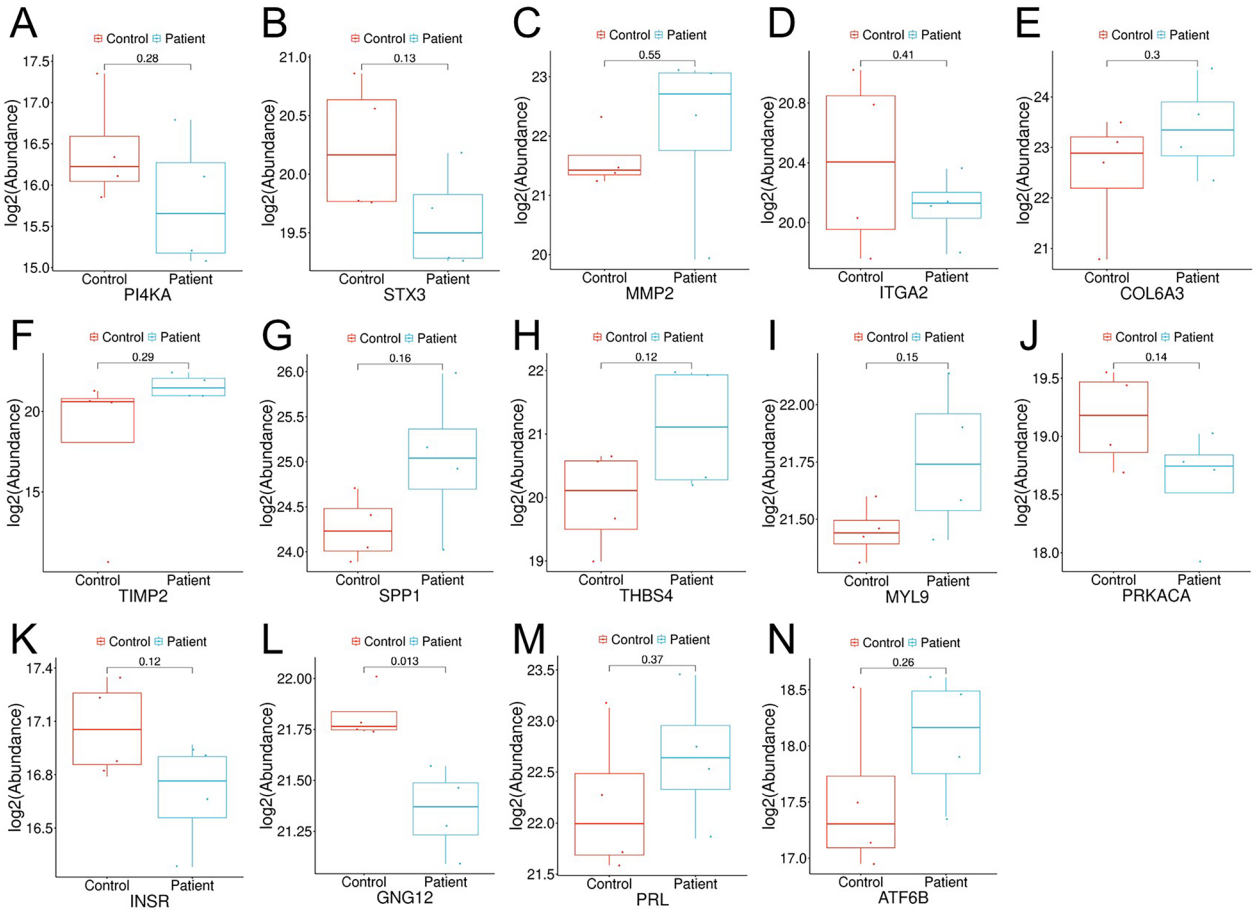

Fig. 7 Validation of proteomic alterations using PRM. Boxplots showing the relative abundance (log2 transformed) of 14 selected proteins in the control (n = 4) and patient (n = 4) groups. Although most comparisons did not reach statistical significance owing to the limited sample size of the validation cohort, the expression trends were consistent with the DIA proteomics results. **A**, **B** Downregulation trends of PI4KA and STX3, validating the impairment of the 22q11.2-related pathway and vesicle trafficking. **C**, **N** Expression levels of additional candidates: MMP2 (**C**), ITGA2 (**D**), COL6A3 (**E**), TIMP2 (**F**), SPP1 (**G**), THBS4 (**H**), MYL9 (**I**), PRKACA (**J**), INSR (**K**), GNG12 (**L**), PRL (**M**), and ATF6B (**N**). *P*-values are indicated above the brackets

Proteomic analysis revealed that differentially expressed proteins were significantly enriched in vascular development, angiogenesis, and the PI3K-Akt signaling pathway. These pathways are fundamental to fetal cardiovascular development. The PI3K-Akt signaling axis is a master regulator of cardiomyocyte proliferation and plays an indispensable role in the remodeling of the cardiac outflow tract [31, 32]. Similarly, coordinated angiogenesis is required for the separation and partitioning of the great vessels [33]. We propose that this pathway dysregulation could be a direct downstream consequence of abnormal vesicular transport. The accumulation of the scaffold SQSTM1 (indicating stalled flux) contrasts with the depletion of its partners, CCM2 and PDCD10. This uncoupling, combined with the sequestration of ADAM10, implies a suppression of pro-angiogenic signaling. Previous studies have established that the CCM signaling complex is indispensable for endothelial junction stability and cardiac morphogenesis [34], while ADAM10-mediated Notch signaling is a prerequisite for coronary vessel differentiation and outflow tract development [35]. The failure to properly transport these pro-angiogenic cargoes could thereby impair vascular remodeling capabilities, providing a plausible molecular explanation for the specific conotruncal anomalies observed in the 22q11.2DS population.

The limitations of this study stem from the inherent challenges in investigating rare prenatal conditions. First, the sample size was restricted (n = 5 per group) due to the extreme scarcity of available amniotic fluid samples from confirmed 22q11.2DS pregnancies. Although the robust separation demonstrated by PCA and hierarchical clustering partially mitigated this limitation, the limited cohort size poses an inherent risk of false positives in identifying differentially expressed proteins, underscoring the necessity for validation in larger, independent multicenter cohorts. Second, the control group comprised pregnancies with indications such as advanced maternal age and in vitro fertilization (IVF). Although these controls were confirmed as chromosomally normal,

the possibility that these clinical variables introduced subtle confounding effects on the exosomal lipidomic and proteomic signatures cannot be entirely excluded. Third, the mechanistic links between lipid remodeling and SNARE trafficking are currently inferred solely from observational multiomics associations. Functional rescue experiments were infeasible in the current study because of the ethical and practical constraints associated with obtaining viable fetal cells directly from amniotic fluid. Consequently, our findings establish strong associations but cannot definitively confirm direct causality between *PI4KA* haploinsufficiency, lipidome remodeling, and SNARE trafficking defects.

Future research should prioritize clinical validation and mechanistic investigation. First, to enhance statistical power and robustly validate the identified multiomic profiles, clinical sample sizes will be expanded through larger, independent multicenter cohorts. Second, functional experiments are essential for establishing causal relationships. Specifically, in vitro rescue assays utilizing *PI4KA* knockdown and overexpression models in relevant cell lines—such as amniotic fluid stem cells or cardiovascular progenitor cells—will evaluate the impact of PI4KA expression levels on membrane biophysics, lipid composition, and vesicular fusion efficiency. Furthermore, established animal models of 22q11.2DS will be utilized to elucidate how the observed exosomal trafficking defects perturb pro-angiogenic signaling and contribute to cardiovascular malformations in vivo. Ultimately, the integration of independent lipidomic and proteomic datasets in this study provides compelling evidence for the membrane curvature trafficking model, serving as a foundational multiomic resource for future targeted interventions.

Conclusion

This study presents the first integrated multi-omic landscape of amniotic fluid exosomes in fetal 22q11.2DS. Our findings indicate that, despite unaltered exosomal morphology, profound molecular remodeling occurs, characterized by specific lipid depletion and widespread protein alterations—notably PI4KA downregulation and SNARE-mediated vesicular transport perturbations. Although these multi-omic associations do not establish direct causality, they provide a novel, hypothesis-driven model suggesting that lipid signaling and vesicular trafficking defects may operate in parallel with or downstream of *TBX1* haploinsufficiency. This research serves as a foundational resource for understanding fetal 22q11.2DS pathophysiology and identifies membrane lipid metabolism as a promising focus for future functional validation and targeted therapeutic exploration.

Abbreviations

22q11.2DS	22Q11.2 Deletion syndrome
AF	Amniotic fluid
AF-Exos	Amniotic fluid exosomes
TEM	Transmission electron microscopy
DLS	Dynamic light scattering
DIA	Data-independent acquisition
PRM	Parallel reaction monitoring
DEPs	Differentially expressed proteins
DELs	Differentially expressed lipids
DG	Diacylglycerols
TG	Triacylglycerols
Cer	Ceramides
PPI	Protein–protein interaction
GO	Gene Ontology
KEGG	Kyoto encyclopedia of genes and genomes
GSEA	Gene set enrichment analysis
PCA	Principal component analysis
CMA	Chromosomal microarray analysis
PI4KA	Phosphatidylinositol 4-kinase alpha
SNARE	Soluble N-ethylmaleimide-sensitive factor attachment protein receptor

Supplementary Information

The online version contains supplementary material available at https://doi.org/10.1186/s40246-026-00963-6.

Additional file 1.

Additional file 2.

Acknowledgements

During the preparation of this work, the authors used Gemini 3.0PRO in order to improve the readability and language quality. The authors reviewed and edited the content as needed and take full responsibility for the content of the publication.

Author contributions

HX, TL, and MZ were responsible for data curation, omics data analysis, and writing the original draft. XL and YG performed the isolation and identification of exosomes. ZG and HW were responsible for data visualization. LG, HL, and SL contributed to clinical sample collection. DW conceived and designed the study and reviewed the manuscript. All authors have read and agreed to the published version of the manuscript.

Funding

This work was funded by the Open Research Fund of NHC Key Laboratory of Birth Defects Prevention (Grant No. NHCKLBDP2024013), the Henan Provincial Science and Technology Tackling Program (Grant No. 252102311131), the Henan Provincial Medical Science and Technology Tackling Program—Province-Ministry Co-construction Key Project (Grant No. SBGJ202402005), and the Henan Province Medical Science and Technology Research Project (Grant Nos. LHGJ20240001, LHGJ20240004, LHGJ20250008).

Data availability

The proteomics datasets generated during the current study are available in the iProX repository (https://www.iprox.cn) under the identifier **PXD073321**. The lipidomics datasets are available in the OMIX database (https://ngdc.cncb.ac.cn/omix) under the accession number **OMIX014514**.

Declarations

Ethics approval and consent to participate

Ethical approval was obtained from the Ethics Committee of Henan Provincial Peoples Hospital, China (No. 2019-134). Written informed consent was obtained from all the participants.

Consent for publication

Not applicable.

Competing interests
The authors declare no competing interests.

Received: 24 January 2026 / Accepted: 29 March 2026
Published online: 08 April 2026

References

1. Scheuerle AE, Geleske TA, Merchant N, Goldenberg PC, Council on G. Health supervision for children with 22q11.2 deletion syndrome: clinical report. Pediatrics. 2025. https://doi.org/10.1542/peds.2025-072717.
2. Korteling D, et al. Untargeted metabolic analysis in dried blood spots reveals metabolic signature in 22q11.2 deletion syndrome. Transl Psychiatry. 2022;12:97. https://doi.org/10.1038/s41398-022-01859-4.
3. Bhalla P, et al. Mesenchymal cell replacement corrects thymic hypoplasia in murine models of 22q11.2 deletion syndrome. J Clin Investig. 2023. https://doi.org/10.1172/JCI173145.
4. Freud LR, et al. Prenatal vs postnatal diagnosis of 22q11.2 deletion syndrome: cardiac and noncardiac outcomes through 1 year of age. Am J Obstet Gynecol. 2024;230:368 e361-368 e312. https://doi.org/10.1016/j.ajog.2023.09.005.
5. De Bono C, et al. Single-cell transcriptomics uncovers a non-autonomous Tbx1-dependent genetic program controlling cardiac neural crest cell development. Nat Commun. 2023;14:1551. https://doi.org/10.1038/s41467-023-37015-9.
6. Nomaru H, et al. Single cell multi-omic analysis identifies a Tbx1-dependent multilineage primed population in murine cardiopharyngeal mesoderm. Nat Commun. 2021;12:6645. https://doi.org/10.1038/s41467-021-26966-6.
7. Gerli MFM, et al. Single-cell guided prenatal derivation of primary fetal epithelial organoids from human amniotic and tracheal fluids. Nat Med. 2024;30:875–87. https://doi.org/10.1038/s41591-024-02807-z.
8. Chen C, et al. Exosomes: new regulators of reproductive development. Mater Today Bio. 2023;19:100608. https://doi.org/10.1016/j.mtbio.2023.100608.
9. Manni G, et al. Amniotic fluid stem cell-derived extracellular vesicles educate type 2 conventional dendritic cells to rescue autoimmune disorders in a multiple sclerosis mouse model. J Extracell Vesicles. 2024;13:e12446. https://doi.org/10.1002/jev2.12446.
10. Gallo DM, et al. Meconium-stained amniotic fluid. Am J Obstet Gynecol. 2023;228:S1158–78. https://doi.org/10.1016/j.ajog.2022.11.1283.
11. Del Rivero T, Milberg J, Bennett C, Mitrani MI, Bellio MA. Human amniotic fluid derived extracellular vesicles attenuate T cell immune response. Front Immunol. 2022;13:977809. https://doi.org/10.3389/fimmu.2022.977809.
12. Senesi G, et al. Extracellular vesicles from II trimester human amniotic fluid as paracrine conveyors counteracting oxidative stress. Redox Biol. 2024;75:103241. https://doi.org/10.1016/j.redox.2024.103241.
13. Medina M, et al. Surface morphometrics reveals local membrane thickness variation in organellar subcompartments. J Cell Biol. 2026. https://doi.org/10.1083/jcb.202505059.
14. Liu C, et al. Identification of the SNARE complex that mediates the fusion of multivesicular bodies with the plasma membrane in exosome secretion. J Extracell Vesicles. 2023;12:e12356. https://doi.org/10.1002/jev2.12356.
15. Cao L, et al. The trajectory of vesicular proteomic signatures from HBV-HCC by chitosan-magnetic bead-based separation and DIA-proteomic analysis. J Extracellular Vesicles. 2024;13:e12499. https://doi.org/10.1002/jev2.12499.
16. Elizarraras JM, et al. WebGestalt 2024: faster gene set analysis and new support for metabolomics and multi-omics. Nucleic Acids Res. 2024;52:W415–21. https://doi.org/10.1093/nar/gkae456.
17. Liu CH, et al. LipidSig 2.0: integrating lipid characteristic insights into advanced lipidomics data analysis. Nucleic Acids Res. 2024;52:W390–7. https://doi.org/10.1093/nar/gkae335.
18. Liu CH, et al. LipidSigR: a R-based solution for integrated lipidomics data analysis and visualization. Bioinform Adv. 2025;5:vbaf047. https://doi.org/10.1093/bioadv/vbaf047.
19. Pang Z, et al. MetaboAnalyst 6.0: towards a unified platform for metabolomics data processing, analysis and interpretation. Nucleic Acids Res. 2024;52:W398–406. https://doi.org/10.1093/nar/gkae253.
20. Welsh JA, et al. Minimal information for studies of extracellular vesicles (MISEV2023): from basic to advanced approaches. J Extracell Vesicles. 2024;13:e12404. https://doi.org/10.1002/jev2.12404.
21. Purow J, Waidner L, Ale H. Review of the pathophysiology and clinical manifestations of 22q11.2 deletion and duplication syndromes. Clin Rev Allergy Immunol. 2025;68:23. https://doi.org/10.1007/s12016-025-09035-4.
22. Zhong L, et al. The TBX1/miR-193a-3p/TGF-beta2 axis mediates CHD by promoting ferroptosis. Oxid Med Cell Longev. 2022;2022:5130546. https://doi.org/10.1155/2022/5130546.
23. Doumane M, et al. Inducible depletion of PI(4,5)P(2) by the synthetic iDePP system in Arabidopsis. Nat Plants. 2021;7:587–97. https://doi.org/10.1038/s41477-021-00907-z.
24. Kim D, Lee S, Jun Y, Lee C. Nir2 crystal structures reveal a phosphatidic acid-sensing mechanism at ER-PM contact sites. Proc Natl Acad Sci USA. 2025;122:e2516849122. https://doi.org/10.1073/pnas.2516849122.
25. McMahon HT, Gallop JL. Membrane curvature and mechanisms of dynamic cell membrane remodelling. Nature. 2005;438:590–6. https://doi.org/10.1038/nature04396.
26. Mangiarotti A, et al. Lipid packing and cholesterol content regulate membrane wetting and remodeling by biomolecular condensates. Nat Commun. 2025;16:2756. https://doi.org/10.1038/s41467-025-57985-2.
27. Pabst G, Keller S. Exploring membrane asymmetry and its effects on membrane proteins. Trends Biochem Sci. 2024;49:333–45. https://doi.org/10.1016/j.tibs.2024.01.007.
28. Bhaskar BR, et al. Differential SNARE chaperoning by Munc13-1 and Munc18-1 dictates fusion pore fate at the release site. Nat Commun. 2024;15:4132. https://doi.org/10.1038/s41467-024-46965-7.
29. Cen J, et al. YKT6 is essential for male fertility by promoting meiosis progression during spermatogenesis of mice. Cell Prolif. 2026;59:e70079. https://doi.org/10.1111/cpr.70079.
30. Arya SB, Collie SP, Parent CA. The ins-and-outs of exosome biogenesis, secretion, and internalization. Trends Cell Biol. 2024;34:90–108. https://doi.org/10.1016/j.tcb.2023.06.006.
31. Lin Y, et al. Neomycin affects cardiovascular and hematopoietic system via the PI3K/Akt pathway in zebrafish larvae. Ecotoxicol Environ Saf. 2025;296:118203. https://doi.org/10.1016/j.ecoenv.2025.118203.
32. Jiang Y, Zhao X, Chen J, Aniagu S, Chen T. PM2.5 induces cardiac malformations via PI3K/akt2/mTORC1 signaling pathway in zebrafish larvae. Environ Pollut. 2023;323:121306. https://doi.org/10.1016/j.envpol.2023.121306.
33. Wu B, et al. Endocardial cells form the coronary arteries by angiogenesis through myocardial-endocardial VEGF signaling. Cell. 2012;151:1083–96. https://doi.org/10.1016/j.cell.2012.10.023.
34. Zhou Z, et al. The cerebral cavernous malformation pathway controls cardiac development via regulation of endocardial MEKK3 signaling and KLF expression. Dev Cell. 2015;32:168–80. https://doi.org/10.1016/j.devcel.2014.12.009.
35. Farber G, et al. ADAM10 controls the differentiation of the coronary arterial endothelium. Angiogenesis. 2019;22:237–50. https://doi.org/10.1007/s10456-018-9653-2.

Publisher's Note